AIAA JOURNAL
Vol. 48, No. 8, August 2010

Combination of Image Postprocessing Tools to Identify Coherent Structures of Premixed Flames

Arnaud Lacarelle,* Dirk M. Luchtenburg,† and Mirko R. Bothien†
Technische Universität Berlin, D-10623 Berlin, Germany
Bernd R. Noack‡
Institut Pprime, F-86036 Poitiers, France
and
Christian O. Paschereit§
Technische Universität Berlin, D-10623 Berlin, Germany

DOI: 10.2514/1.J050188

A combination of postprocessing tools of OH*-chemiluminescence snapshots is used to characterize the coherent structures of two types of premixed burners: a bluff body and an industrial swirl burner. Two methods are combined to extract the structures: a phase-averaging algorithm and the proper orthogonal decomposition. The first method is based on the estimation of the instantaneous phase of the snapshots relative to a (local) time-resolved signal. A phase-sorting–phase-averaging algorithm then reconstructs the evolution of the flame at a chosen frequency over one cycle. The proper orthogonal decomposition method is used as a filter to smoothen the snapshots. Both methods provide insight into the physical mechanisms of coherent structures in the two premixed flames under consideration. The snapshots of the bluff-body combustion exhibit a symmetric structure. This indicates that the von Kàrmàn vortex street in the cold flow is suppressed by the addition of heat in the shear layer. Three coexisting flame structures of the swirl burner in the combustion chamber could be identified: a natural helical structure of the burner and two axisymmetric modes. Increasing the amplitude of acoustic forcing at the natural flow frequency changes the helical structure to an axisymmetric one.

I. Introduction

LEAN-PREMIXED combustion was introduced approximately 20 years ago by the manufacturers of land-based gas turbines in order to fulfill stringent exhaust gas restrictions. In the near future, even stricter emission guidelines will most probably force the aeroengine industry also to move toward this technology. The major constraints for implementation of lean-premixed combustion here are thermoacoustic pulsations, which have been the subject of intensive research for more than 50 years [1,2].

Thermoacoustic oscillations can occur if the unsteady heat release fluctuates in phase with pressure oscillations inside the combustor. Many single mechanisms play a governing role in the onset of thermoacoustic instability, all resulting from the complex interaction mechanisms between fluid dynamics, acoustics, and heat release [3]. Large-scale coherent structures are known to be one of the major drivers of those combustion instabilities, both in premixed and nonpremixed combustion systems [4–6]. By inducing strong local velocity oscillations, they can influence the fuel/air mixing upstream of the flame or the mixing of fresh gases with the reaction products in recirculation zones [7]. Reaching the flame front, they create hot spots or change the flame surface area. The induced periodical heat release fluctuations may excite acoustic modes of the combustor, and hence cause strong pressure oscillations.

Received 4 September 2009; revision received 15 February 2010; accepted for publication 19 February 2010.

*Ph.D. Student, Institut für Strömungsmechanik und Technische Akustik (Corresponding Author).
†Ph.D. Student, Institut für Strömungsmechanik und Technische Akustik.
‡Research Director, CNRS–Université de Poitiers–ENSMA, UPR 3346, Département Fluides, Thermique, Combustion.
§Professor, Institut für Strömungsmechanik und Technische Akustik. Senior Member AIAA.

The generation of strong dominant coherent structures is characteristic of swirling flows combined with sudden area expansions; the latter being a typical feature for modern lean-premixed combustors. A combination of helical structures with axisymmetric vortex shedding is obtained [5], and control or suppression of such large-scale vortices can lead to benefits regarding stability and NO_x emissions [8,9].

The interaction of the coherent structures with a flame depends on the nature of the flow structure itself. While helical structures remain present in reacting unstable flows [10], theoretical and experimental investigations performed on simple bluff-body burners show that Kelvin–Helmholtz antisymmetric vortices are dampened, and a symmetric structure dominates the combustion zone [11]. To validate and investigate the behavior of such structures experimentally, it is relevant to obtain more information on their nature and their response to varying acoustic forcing used to simulate combustion instabilities. One of the fastest ways to obtain this information is the use of a camera, which acquires the line-of-sight heat release of the flame on a two-dimensional (2-D) charge-coupled device (CCD) chip. Thus, at each pixel location, an integral value of the heat release is acquired. The disadvantages of the 2-D integral acquisition become evident when the flame and its structures are strongly three-dimensional (3-D). In this case, the commonly used reverse Abel transformation would fail to describe the flowfield on the symmetry axis of the flame properly, as the flame cannot be considered to be rotationally symmetric. A 3-D reconstruction of the flame based on tomographic image processing is possible using many cameras simultaneously [12], but a good optical access to the flame from numerous viewing angles is required, and the postprocessing remains all but trivial. The use of planar laser-induced fluorescence allows the recording of the flame shape in a 2-D plane but is an expensive technique both in time and cost. It is, thus, necessary to develop tools that can be used to analyze and reconstruct the dominant flow structures captured by 2-D integral images.

Regarding experimental measurement campaigns, one would like to obtain the maximum information on a system within a minimum amount of measurement time. This can be achieved by suitable postprocessing methods of simultaneously recorded data as time

signals of pressure oscillations and pictures recorded by the camera. One commonly used tool to identify the dominant modes of a flow is based on the proper orthogonal decomposition (POD) of a series of data. This method is, for instance, applied to numerical and experimental data sets [13,14] to extract the flow structures of interest by filtering out turbulence or other modes. POD analysis of combustion processes is a powerful means to gain physical insight of combustion/flame dynamics and coherent structures, as was, for example, also pointed out in the numerical work of Edwards et al. [15]. In the literature, most of the POD work performed on experimental data comes from 2-D-planar measurements, where a flow property (concentration or velocity) acquired by the camera corresponds to one spatially well-defined location. However, to the knowledge of the authors, this method was, until now, not applied on experimental records integrating one flow property, along a line of sight, as the heat release of a flame recorded by a camera. The use of the POD or Fourier filtering is, thus, of interest to gain more information from integral flame visualization.

Besides the shapes of the modes, instantaneous phase information of the image captured is also needed to allow for a phase reconstruction of the modes. Many methods can be found in the literature to extract the instantaneous phase of a periodic signal. However, to obtain satisfying results, filtering of the signal is, in most cases, necessary, as signals from the experiment are disturbed by noise or dominant frequencies, which have to be filtered out. Phase information can then be gained with simple methods from the Lissajou figures or zero-crossing phase meters to more complex fast-Fourier-transform (FFT)-based methods. An elegant method was first proposed by Gabor [16] who obtained the phase of a real-time signal $s(t)$ by using the Hilbert transformation. Güthe and Schuermans [17] applied this method successfully to obtain the instantaneous phase of OH*-chemiluminescence snapshots relative to pressure signals. This, associated with a postprocessing sorting algorithm of the snapshots, allows the reconstruction of the phase evolution of different modes of the flame. If no time-resolved signal is available, or when the camera snapshots are temporally uncorrelated, the phase information can be extracted directly from the recorded camera snapshots. Different methods are available, often based again on POD [18,19] or the Karhunen–Loeve decomposition [20]. The advantage of these methods is generally a more accurate phase extraction, but the frequency information is not available as long as no high-speed measurement system is used. Thus, it may be applied in complement to the instantaneous phase extraction previously described.

In the first experimental setup, we focus on the investigation of the flame structures behind a bluff body. Both unforced and forced flames are investigated, and the resulting dominant modes are analyzed by direct phase averaging or phase averaging of POD reconstructed snapshots. Following the results of the bluff-body burner, we investigate the coherent flow structure of an industrial-like (swirl-stabilized) burner, which shows two dominant natural modes: an axial one, defined by the boundary conditions of the test rig, as well as an azimuthal one, induced by the swirling flow. Finally, we investigate the impact of acoustic forcing at different amplitudes on the natural helical mode.

II. Experimental Setups

In this section, the setups of the investigated burners are presented. After this, the combustion chamber and, finally, the measurement equipment are described.

A. Bluff-Body Burner

Figure 1 presents the setup of the bluff-body burner. The bluff body is mounted in a square test section of height $H = 62.5$ mm and width $W = 72$ mm. The ratio of the bluff-body height h to the test-section height is $h/H = 0.4$. The ratio of length l of the bluff body to its height is $l/h = 3$. Upstream of the burner, a plate is used to inject fuel at four different axial positions. At each axial location, 10 equidistantly spaced holes are arranged on both sides of the plate to ensure a symmetrical fuel injection. For the present investigations,

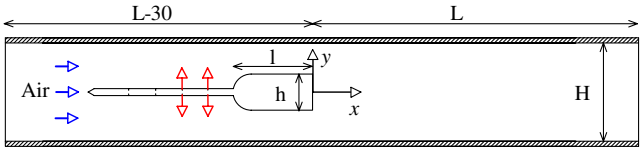

Fig. 1 Sketch of the bluff-body burner.

only two injections located at $-4.16h$ and $-5.36h$ are used, as shown by the vertical arrows in the crossflow in Fig. 1. Measurements performed in reacting flows are conducted at an air mass flow of 120 kg/h, corresponding to a Reynolds number Re based on the bluff-body height and the bulk velocity upstream of the trailing edge of $Re = 15,800$. Even if the boundary conditions due to the casing, as well as the boundary layer on the bluff body, lead to a more complex flow, the dominant coherent flame structures are mostly 2-D and can be used to validate the image postprocessing algorithm.

B. Swirl-Stabilized Burner

A more complex flame structure is achieved with a typical industrial swirl-inducing burner. A schematic of the burner is shown in Fig. 2. The burner consists of two halves of a cone that are shifted with respect to each other in radial direction, such that two inlet slots of constant width are formed. The diameter of each cone half at the outlet is $D = 82$ mm. This diameter is the reference length used to define all characteristic numbers. The airflow through these lateral slots generates a strong tangential velocity component. Because of this component, a flow with a high degree of swirl occurs that, combined with the dump plane at the burner outlet, produces a vortex breakdown and a zone of flow recirculation. A detailed description of the burner is given by Sattelmayer et al. [21] and Doebbeling et al. [22].

Both the cold flow of the swirler, as well as the reacting flow, have been thoroughly investigated in previous studies [5,7,8,10]. Among other relevant results, a natural helical flow structure corresponding to a precessing vortex could be evidenced at the burner outlet in the cold and reacting cases. When the nonreacting flow was acoustically forced at the frequency of the helical structure, a change from a helical to an axisymmetric structure was observed by Lacarelle et al. [7]. The study confirms the previous results of Paschereit et al. [8] in reacting flow, in which the helical structure could be suppressed in the case of forcing at the frequency of the helical mode. For operating conditions of the burner that feature thermoacoustic pulsations, axisymmetric oscillations of the flame could be clearly detected over a wide frequency range. Thus, it is expected to observe these typical structures in the present study as well.

C. Combustion Chamber

The burners are mounted in the same combustion chamber as shown in Figs. 3 and 4. In both cases, a loudspeaker located upstream of the burner is used to force the flow at different frequencies. A microphone, also mounted upstream of the burner, records the pressure oscillations in the combustion chamber. One particularity of

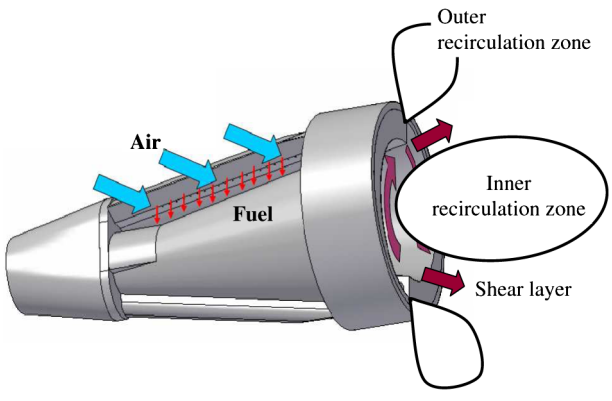

Fig. 2 Picture of the swirl burner.

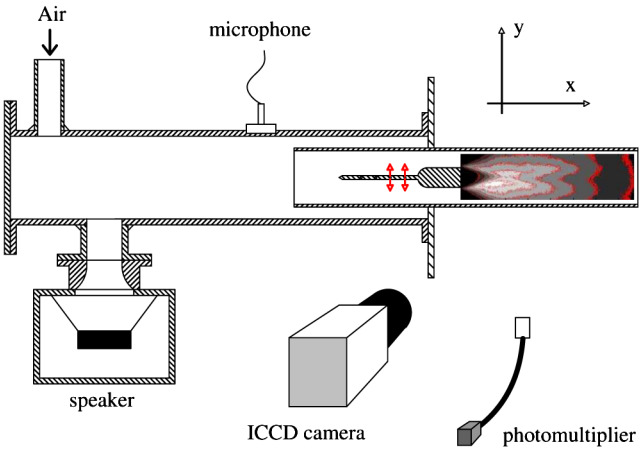

Fig. 3 Measurement setup for the bluff-body burner.

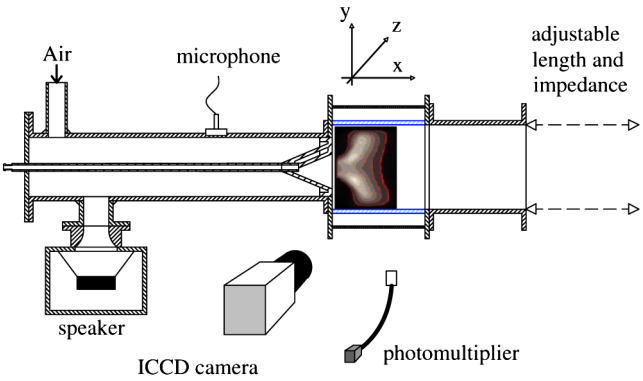

Fig. 4 Measurement setup for the swirl burner.

the investigations performed with the swirling flow burner is that the reflection coefficient at the outlet of the combustion chamber can be actively controlled. By adjusting the controller appropriately, the magnitude and phase of the downstream reflection coefficient can arbitrarily be tuned, resulting in a desired adjustment of the thermoacoustic feedback cycle. In this way, the amplitude of the first resonance mode of the combustor, corresponding to a quarter-wave mode, can be dampened, mitigating the strength of this mode, relative to others. In this way, three modes, equivalent in strength, can coexist. More details on the control scheme are given by Bothien et al. [23].

D. Measurement Equipment

The same measurement equipment is used for both burners considered. An intensified CCD (ICCD) camera equipped with a UV lens and a 312 nm bandpass filter records the OH^* chemiluminescence of the flame. The shutter time is set to 0.1 ms, corresponding to an angle resolution of 7 deg at a frequency of 200 Hz. The camera frame rate is set around 6 Hz, which is far below the Nyquist criterion, to capture the typical frequencies of the system, ranging from 50 to 200 Hz. This can only be done with an adequate postprocessing. For this, the signal of the CCD chip exposure is recorded in the same time with the signals of the microphone and a photomultiplier, which records the global OH^* chemiluminescence through a bandpass filter centered around 308 nm. A maximum of 500 pictures per series are acquired for the different configurations. As shown in previous works [7], a relative low number of snapshots N allows the catching of dominant flow structures ($N < 500$). Thus, to reduce the amount of data and shorten the recording time, a series of 280 pictures are acquired for some cases of the forced swirling flow.

The signal-to-noise ratio (SNR) of the pictures was estimated to be typically $\mathrm{SNR}_{\mathrm{single}} \approx 0.52$ for single images, and $\mathrm{SNR}_{\mathrm{average}} \approx 3.1$ for an average picture made of 35 snapshots (see Dussault and Hoess [24] for the calculation method). This SNR will vary, depending on the local intensity recorded, being higher when high-intensity events are recorded and vice versa. This theoretical calculation points out that the OH^* signal remains extremely noisy, and interpretation of single snapshots is possible but must be done with caution. Only averaged pictures show a sufficient SNR (even if very low) to lead to a nonambiguous interpretation of the recorded structures.

As stated in [25,26], the OH^* signal recorded by the camera or photomultiplier cannot be directly considered as a quantitative measure of the flame heat release. However, the relationship

$$\mathrm{OH}^* \propto m_{\mathrm{air}} \phi^b \tag{1}$$

where m_{air} is the air mass flow, ϕ the equivalence ratio, and b is a constant fulfilling $b > 1$ is reported by several authors [27–29] investigating the global chemiluminescence response of a premixed flame. This correlation is optimum when the broadband $CO2^*$ emission is subtracted from the total emissions recorded around the wavelength of 308 nm. Such a correction for a complex 3-D flame remains complex and is not applied here. Thus, only a qualitative evaluation of the fluctuations can be achieved. The recorded image intensity ($\mathbf{Q}$) reads as:

$$\mathbf{Q}(\mathbf{x}, t) = \mathrm{OH}^*(\mathbf{x}, t) + \mathrm{CO2}^*(\mathbf{x}, t) \tag{2}$$

and, regarding local normalized oscillations in Eq. (2), becomes

$$\frac{\mathbf{Q}(\mathbf{x}, t)'}{\overline{\mathbf{Q}(\mathbf{x}, t)}} = \frac{\mathrm{OH}^{*\prime}(\mathbf{x}, t) + \mathrm{CO2}^{*\prime}(\mathbf{x}, t)}{\overline{\mathbf{Q}(\mathbf{x}, t)}} \tag{3}$$

Steady calibration maps [30] show that the sign of $OH^{*\prime}$ and $CO2^{*\prime}$ are the same, so that positive oscillations recorded by the camera are partially a result of positive fluctuations of the local $OH^{*\prime}$ chemiluminescence. Even if local oscillations of the flame area or density may influence these emissions, it is reasonable to assume that a strong part of these emissions results from fluctuations of the equivalence ratio ϕ' or of the air mass flow m'_{air}. In the case of the swirl-stabilized burner, nonreacting high-speed concentration measurements [31] indicate that coherent and large-scale fuel pocket fluctuations are present at the burner outlet and can be considered, in the present case, as the major source of $OH^{*\prime}$ fluctuations. However, no quantitative information on the heat release or temperature can be extracted without further equipment.

To validate the results obtained from the camera snapshots with the swirl burner, two photomultipliers integrating the flame light over one line of sight of around 10 mm diameter and equipped with bandpass UV filters (295–385 nm, U340) are used, as presented in Fig. 5. The photomultipliers are placed on both sides of the burner. Both photomultipliers are mounted at a streamwise position of

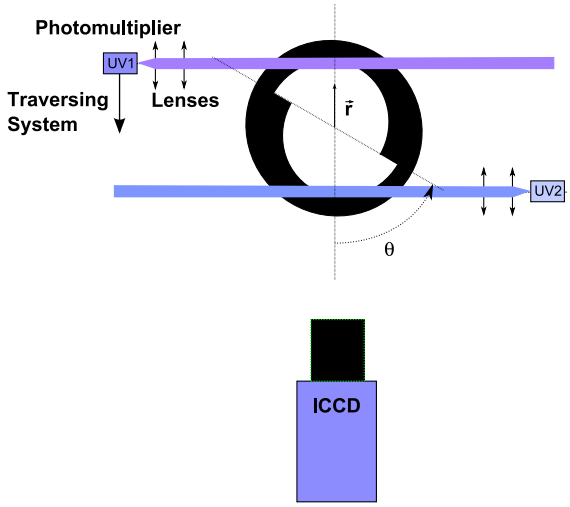

Fig. 5 Schematic of the photomultiplier positions and angle of view of the camera θ relative to the slots of the swirl burner (top view).

$x/D = 0.3$. One of the photomultipliers is mounted at a defined radial position ($r/D = 0.4$), while the second can be traversed perpendicular to the line of sight of the first one. By calculating the phase and amplitude of the coherence function between both signals, a verification of the mode shape can be achieved.

III. Data Analysis Techniques

As previously mentioned, the camera frame rate does not allow for a time-resolved acquisition of the flame dynamics. Thus, a post-processing phase sorting of the pictures is needed. The phase extraction of a signal is presented in Sec. III.A. POD is used to filter the snapshots and extract the coherent structures (Sec. III.B). The raw or POD-filtered snapshots are then phase averaged to allow for flame structure visualization at different frequencies of interest (last section).

A. Signal Filtering and Phase Extraction

Figure 6 shows two typical spectra of pressure and integral OH* signals obtained for the swirl burner when acoustic forcing is applied upstream of the flame. In this case, three modes dominate the combustion process. The mode corresponding to the frequency peak at $f = 75$ Hz is the quarter-wave mode of the combustion chamber. The peak at 150 Hz is the frequency of acoustic forcing. Both modes are expected to induce axisymmetric changes in the flame shape as they induce periodical oscillations of the mean axial velocity in the combustion chamber. The third mode, around 170 Hz, represents the natural flow frequency.

Since these different modes are recorded simultaneously by the pressure sensors, a proper filtering of the signal is required to obtain the phase reconstruction of each mode and to allow the sorting of the OH* snapshots. Different methods can be used to extract the instantaneous phase of the time signal. In the present work, a filter in the frequency domain, as well as a Hilbert transformation in the time domain, are used, as illustrated in Fig. 7. The time signal of interest $s(t)$ (pressure or OH* recorded by the photomultiplier) is first Fourier transformed, giving $\hat{s}$, with the $\widehat{(\cdot)}$ denoting the Fourier transform. This is then filtered in the frequency domain with a bandpass zero phase-shift filter, resulting in $\hat{s}_f$. The latter is converted back into the time domain through an inverse FFT, giving s_f. The Hilbert transformation (which, for pure harmonic signals, can be seen as a phase shifting of $-\pi/2$) is then applied to the filtered signal. The complex phasor z, which contains the amplitude and phase information, is obtained after summation of the signal s_f and its Hilbert transform multiplied by the complex number j. Finally, the complex signal z can be used to phase sort the trigger signal of the camera. A detailed description of this method is presented by Güthe and Schuermans [17]. The only free parameter of the processing, the width of the bandpass filter, is adjusted, depending on the width of the frequency peak of $\hat{s}_f$.

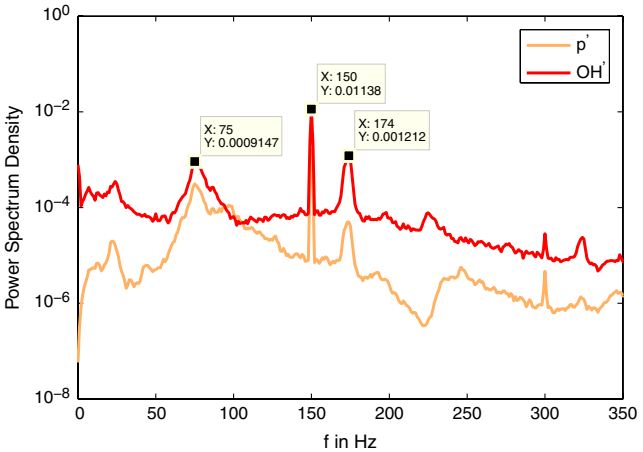

Fig. 6 Typical spectra of pressure and integral OH* signals for the swirl-inducing burner. The OH* signal was recorded without optical arrangement between photomultiplier and flame.

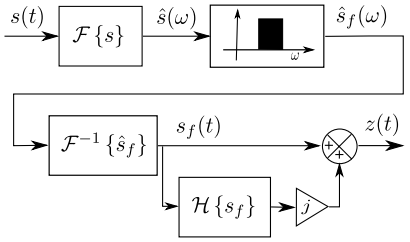

Fig. 7 Signal processing to extract the phase information of a reference signal $s(t)$. The resulting complex phasor is $z(t)$.

The phase-sorting algorithm was first tested with generic signals; a linear combination of two pure sinusoidal signals at 200 and 40 Hz, on which a 10% Gaussian noise N is superposed, simulates the reference signal $s(t)$. A square signal with a 10% duty cycle and a frequency of 4.55 Hz simulates the camera trigger. The instantaneous phase of the signal, relative to one of the frequencies, can be directly calculated and compared with the phase obtained after processing, following Fig. 7. The comparison between the two values is illustrated in Fig. 8 and shows that the theoretical and reconstructed phase angles match very well, thus validating the algorithm. Furthermore, Fig. 9 shows the result for the application of the filter on a reference signal for two frequencies, shown in Fig. 6, and for an arbitrary one. The plots show that, for the two combustor modes (upper graphs), the algorithm extracts the corresponding oscillation frequency very well, which approximates a sinusoid. The phase of the signal filtered is identical to that of the original signal and is consecutive to the zero phase-shift filtering (see filtered signals at 75 and 150 Hz). In the case of signal processing at a frequency that does not dominate the system dynamics (50 Hz, lower graph), the filtered signal shows a weak oscillation only.

B. Proper Orthogonal Decomposition Analysis of the Snapshots

The snapshots acquired with the ICCD camera are 2-D recordings of the flame shape projected on the (x, y) plane along the z axis and taken at the time t_l. They are also called raw snapshots and denoted as $\mathbf{Q}(\mathbf{x}, t_l)$, with $\mathbf{x} = (x, y)$. As stated before, POD can be applied to extract coherent structures from such image series. Here, each image is decomposed into the mean and a fluctuation part, which reads as

$$\mathbf{Q}(\mathbf{x}, t_l) = \overline{\mathbf{Q}(\mathbf{x}, t_l)} + \sum_{i=1}^{N} a_i(t_l)\mathbf{Q}_i(\mathbf{x}) \tag{4}$$

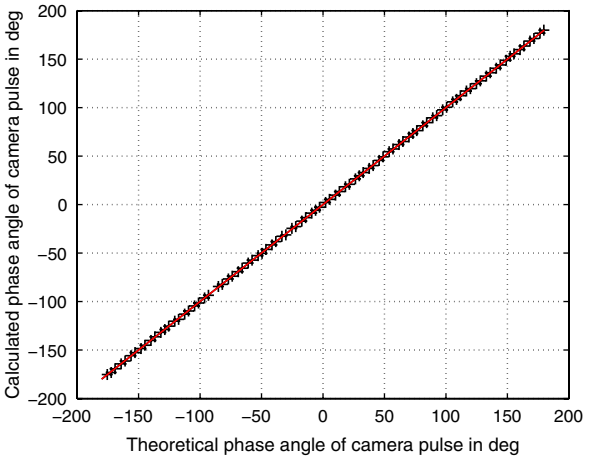

Fig. 8 Comparison of the theoretical angle of a simulated camera trigger with the angle obtained after processing, following Fig. 7; $s(t) = 0.5[\sin(2\pi \cdot 200t) + \sin(2\pi \cdot 40t)] + 0.1N(t)$ (N Gaussian noise), square camera trigger of frequency 4.55 Hz and duty cycle 10%, filter centered on 40 Hz, and bandpass 5 Hz.

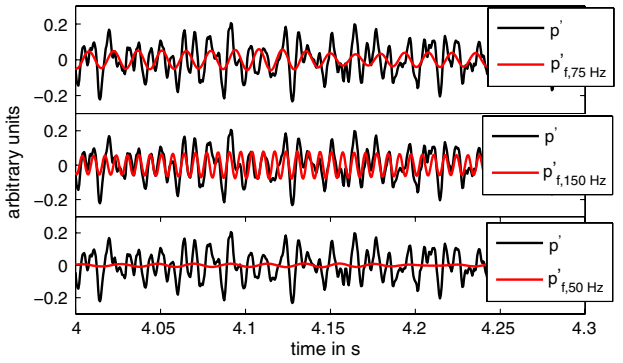

Fig. 9 Comparison of pressure signals without and with a bandpass filter centered on the mode frequencies of 75 (top) and 150 Hz (middle) (see also Fig. 6) and an arbitrarily chosen frequency of 50 Hz (bottom).

where $\overline{\mathbf{Q}(\mathbf{x}, t_l)}$ denotes the ensemble average of $\mathbf{Q}(\mathbf{x}, t_l)$, $\mathbf{Q}_i$ is a mode, and a_i a mode amplitude.

The modes are obtained by maximizing the variance of the data set. This is mathematically expressed as follows:

$$\arg\max_{\mathbf{Q}_i}; \qquad \frac{\overline{|(\mathbf{Q}, \mathbf{Q}_i)|^2}}{\|\mathbf{Q}_i\|^2} \tag{5}$$

where $(\cdot, \cdot)$ is the standard $\mathcal{L}_2$ inner product, $\|\cdot\|$ is the corresponding norm, and $|\cdot|$ denotes the modulus. This formulation leads to the following eigenproblem:

$$\int_\Omega \overline{\mathbf{Q}(\mathbf{x}, t_l)\mathbf{Q}(\mathbf{x}', t_l)}\mathbf{Q}_i(\mathbf{x}')\, d\mathbf{x}' = \lambda_i \mathbf{Q}_i(\mathbf{x}) \tag{6}$$

where Ω is the spatial domain. Thus, the optimal modes are given by the eigenfunctions of the autocorrelation function. The temporal amplitudes $a_i(t_l)$ are obtained by projection of the snapshots onto the modes. Both the spatial modes $\mathbf{Q}_i$ and the temporal amplitudes a_i are orthogonal. The eigenvalues λ_i are proportional to the contribution of the variance of the modes. A relatively large variance or eigenvalue of a POD mode is usually associated with (without being by itself) a coherent structure. Since the spatial dimension is of the order or of 1 million, the method of snapshots developed by Sirovich [32] is used to compute the POD. More details can be found in the work of Holmes et al. [33].

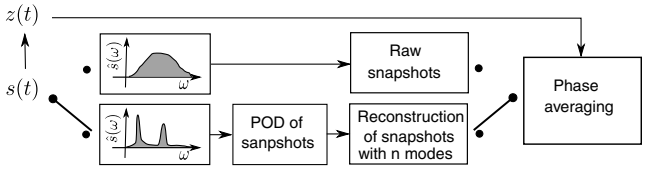

Fig. 10 Scheme of the flowchart for picture processing.

C. Snapshot Processing and Phase Averaging

The power spectra presented in Fig. 6 show different types of modes: sharp peaks at 150 and around 170 Hz and a broader one around 75 Hz. In the case of well-defined frequencies, the POD analysis yields few dominant modes (the $\mathbf{Q}_i$), which are combined to describe the coherent structure evolution and enhance their visualization, as illustrated in Fig. 10. If no distinct frequency peak prevails, then no strong coherent structure is expected. The POD yields modes with similar eigenvalues λ_i, and many of them are needed to reconstruct the flame evolution. In this case, the POD reconstruction will not give further information than the direct phase averaging of the raw snapshots. In both cases, the raw or the reconstructed snapshots need to be phase averaged to reconstruct the mean structure evolution. The procedure is briefly described in the following.

Consider N phase intervals of width $\Delta\phi = 360/N$ equally spaced over one period $[-180; 180]$. The phase interval k that is considered is defined as $[\phi_k, \phi_{k+1}]$, with $\phi_k = -180 + k\Delta\phi$ $(k = 1, 2, \ldots, N)$. One snapshot $\mathbf{Q}(\mathbf{x}, t_l)$ belongs to the phase interval k when the condition $\arg[z(t_l)] \in [\phi_k, \phi_{k+1}]$ is satisfied, where z represents the phasor of the reference signal s, which is used for the reconstruction, and t_l represents the time at which the picture $\mathbf{Q}(\mathbf{x}, t_l)$ was taken. The resulting pictures belonging to the phase k are denoted as $\mathbf{Q}(\mathbf{x}, t_{l,k})$. After phase sorting all of the pictures, the mean picture $\bar{\mathbf{Q}}_k$ of the phase interval k is calculated as $\bar{\mathbf{Q}}_k = \overline{\mathbf{Q}(\mathbf{x}, t_{l,k})}$, with $\overline{(\cdot)}$ being the ensemble-averaging operator over the index l.

To visualize the OH* oscillations relative to the mean flame and to compensate asymmetries, the relative light intensity $\bar{\mathbf{Q}}_k^*$ of the phase interval k is introduced:

$$\bar{\mathbf{Q}}_k^* = \frac{\bar{\mathbf{Q}}_k - \bar{\mathbf{Q}}}{\bar{\mathbf{Q}}} \tag{7}$$

where $\bar{\mathbf{Q}} = \overline{\mathbf{Q}(\mathbf{x}, t_l)}$ is the averaged picture of all the snapshots acquired. Thus, positive values present stronger OH* emissions and negative values a lack in the OH* emissions when compared with the local mean emission.

To interpret the coherent structures quantitatively, the phase-averaged pictures are divided into four equal rectangular planes: upstream ($\mathcal{P}_{\text{up}}$), downstream ($\mathcal{P}_{\text{ds}}$), left ($\mathcal{P}_l$), and right ($\mathcal{P}_r$) of the flame. These regions are shown for both flames in Fig. 11. The light intensity in these planes is calculated and then phase averaged to obtain the OH*-emissions parameter $\overline{q_{k,\mathcal{P}}} = \overline{\langle \mathbf{Q}(\mathbf{x}, t_{l,k}) \rangle_{\mathbf{x}\in\mathcal{P}}}$ and its relative value $\overline{q_{k,\mathcal{P}}}^*$:

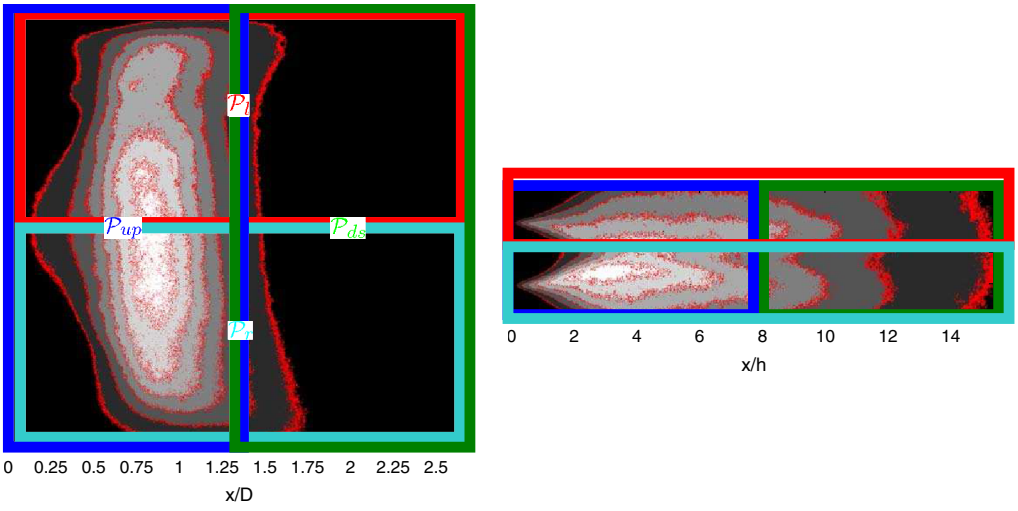

Fig. 11 Visualization of the planes $\mathcal{P}_{\text{up}}$, $\mathcal{P}_{\text{ds}}$, $\mathcal{P}_l$, and $\mathcal{P}_r$, used to calculate the averaged values of $\overline{q_{k,\mathcal{P}}}^*$.

$$\overline{q_{k,\mathcal{P}}}^{\,*} = \frac{\overline{q_{k,\mathcal{P}}} - \bar{q}_{\mathcal{P}}}{\bar{q}_{\mathcal{P}}} \tag{8}$$

where $\bar{q}_{\mathcal{P}} = \overline{\langle \mathbf{Q}(\mathbf{x}, t_l) \rangle_{\mathbf{x}\in\mathcal{P}}}$ is the mean overall OH* emission recorded by the camera over one period. In Fig. 12, the phase-averaged values of the overall OH* chemiluminescence of the camera ($\overline{q_{k,(\mathcal{P}_{up}+\mathcal{P}_{ds})}}$) are compared with the phase-averaged global OH* signal of the photomultiplier. Both sensors have, as expected, the same evolution over one period, with negligible variations. This result validates the phase-averaging and phase-reconstruction procedures.

IV. Coherent Structures of the Bluff-Body Burner

A. Cold-Flow Investigation

In cold flow, and at the Reynolds number of interest $Re = 15,800$, a von Kármán vortex street is expected downstream of the trailing edge. A microphone is placed at $x/l \approx 1$ on the mean axis, and the Reynolds number is varied between 13,000 and 26,000 by changing the air mass flow. The FFT analysis of the signal shows a clear dominant frequency that scales linearly with the bulk velocity. Made dimensionless, the corresponding Strouhal number is equal to $St = 0.27$. The frequency recorded by the microphone is twice the vortex-shedding frequency on one side of the bluff body, so that the common Strouhal number based on the vortex-shedding frequency is equal to $St_s = 0.135$. As the reacting investigations are performed at a mass flow of 120 kg/h, a frequency peak around 57 Hz ($St_s = 0.135$) or at higher harmonics is likely to appear.

B. Reacting Flow

For the reacting case, a normalized equivalence ratio of $\phi = 0.70$ (lean combustion) is adjusted. Figure 13 shows the mean OH* chemiluminescence of the flame downstream of the bluff body. A v-shaped flame is visible, with an OH*-emission maximum located between two and eight burner heights downstream of the trailing edge. The flame appears slightly asymmetric, possibly because of a slightly nonsymmetric fuel injection on both sides of the bluff body.

Figure 14 presents the spectra of the microphone and the OH* photomultiplier for both natural and forced flows. The spectrum of the OH* signal shows a frequency peak around 57 Hz, which corresponds to the expected frequency of the vortex shedding on one side of the bluff body ($St_s = 0.135$). As expected from the broad bandwidth of the OH* signal, the POD analysis of the OH pictures did not reveal any strong dominant structures of the unforced flow, and direct phase averaging of the snapshots was applied. The resulting flame evolution is presented in Fig. 15. The relative phase-averaged OH* emissions $\bar{\mathbf{Q}}_0^*$, $\bar{\mathbf{Q}}_2^*$, $\bar{\mathbf{Q}}_4^*$, and $\bar{\mathbf{Q}}_6^*$, corresponding to the phase intervals $[-180, -135]$, $[-90, -45]$, $[0, 45]$, and $[90, 135]$ are plotted with a black/white scale for clearer visualization. The black color depicts lower OH* emissions than the local mean, the white depicts higher ones. These pictures show a global symmetry of the flame relative to the plane $y/h = 0$, which is confirmed by the relative OH* integrations $\overline{q_{k,\mathcal{P}}}^*$ in the four planes ($\mathcal{P}_{up}, \mathcal{P}_{ds}, \mathcal{P}_l, \mathcal{P}_r$) that oscillate in phase. Furthermore, a closer observation of the phase-averaged pictures ($\bar{\mathbf{Q}}_4^*$ and $\bar{\mathbf{Q}}_6^*$) shows that an oscillation of OH* emissions perpendicular to the flow direction is present. These results confirm previous numerical investigations and a low-order study made on a similar configuration by Li et al. [11], who showed that combustion changes the typical antisymmetric vortex street behind a bluff body to a more symmetric one.

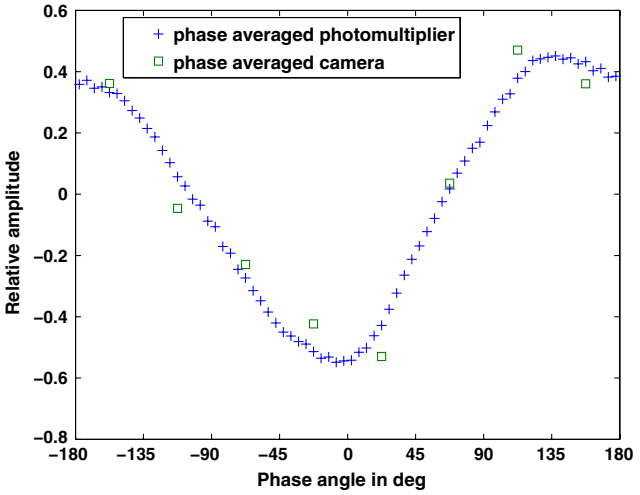

Fig. 12 Comparison of the phase-averaged oscillation of the OH* emissions of the swirl-inducing burner recorded by the photomultiplier (+), with the phase-averaged OH* oscillation recorded by the camera $\overline{q_{k,(\mathcal{P}_{up}+\mathcal{P}_{ds})}}$ (□). The values are scaled by their oscillation amplitudes.

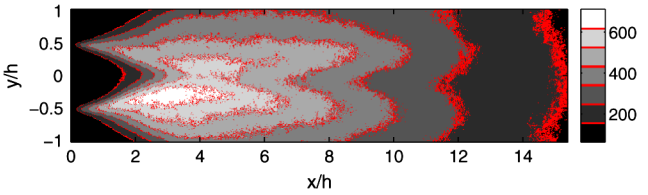

Fig. 13 Mean OH* chemiluminescence of the bluff-body flame, unforced case.

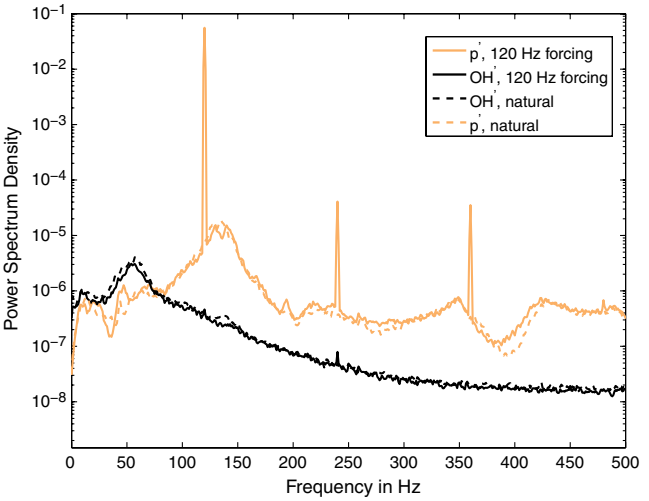

Fig. 14 OH* and pressure spectra of the natural (dotted) and the forced (solid) case.

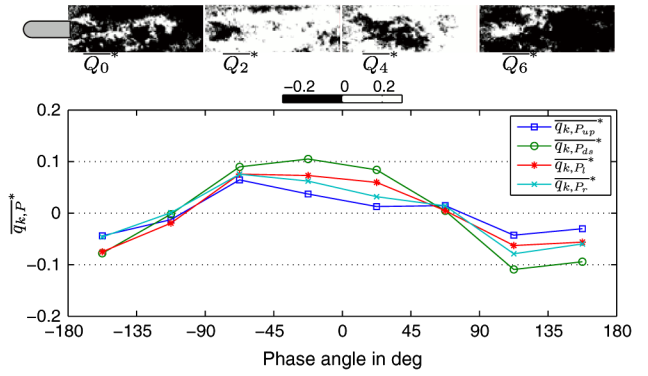

Fig. 15 Phase evolution of the unforced flame around 57 Hz, natural flow. The OH* emissions of the phases $\bar{\mathbf{Q}}_k^*$, with $k = 0, 2, 4, 6$ is shown. Black shows lower-OH* emissions than the local mean, and white shows higher ones. The graph depicts the values of the relative spatially averaged heat release $\overline{q_{k,P}}^*$.

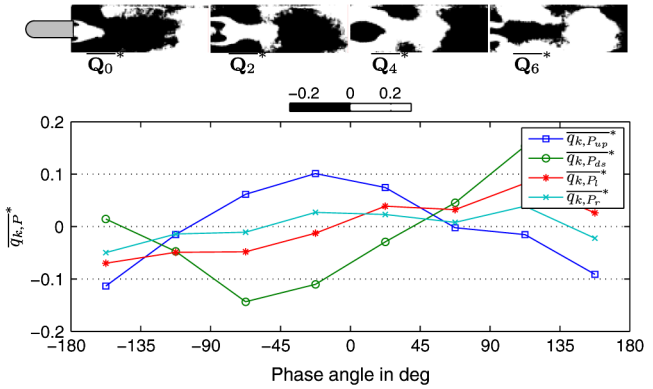

Fig. 16 Phase averaging of the raw snapshots at the forcing frequency, i.e., 120 Hz.

C. Reacting Flow with Acoustic Forcing

Also visible in Fig. 14 is that the global OH* signal from the photomultiplier does not respond to an acoustic forcing at 120 Hz, while the pressure spectrum of p' presents a distinct peak. The results reported in Sec. IV.C.1 show the underlying physical mechanisms. In Sec. IV.C.2, the comparison of the direct phase-averaging processing with the phase average of the POD-reconstructed snapshots is presented.

1. *Phase Averaging of Raw Snapshots at the Forcing Frequency*

The analysis of the forced flame reveals more distinct coherent structures. Phase averaging is performed at the dominant frequency (i.e., 120 Hz). The results are presented in Fig. 16, where four phases ($k = 0, 2, 4, 6$) illustrate the evolution of the structures over one cycle. The flame originates at the trailing edge of the bluff body ($k = 0$). With increasing phase angle, the symmetric structure spreads in the y and x^+ directions ($k = 2$), inducing a maximum of OH* emissions behind the bluff body ($k = 4$). This maximum then moves further downstream and toward the walls ($k = 6$), where it loses its strength ($k = 0$). This structure induces an oscillation of the OH* emissions in the upstream and downstream half planes, as shown by $\overline{q_{k,\mathcal{P}_{up}}}^*$ and $\overline{q_{k,\mathcal{P}_{ds}}}^*$ in Fig. 16 (the relative values presented here show the same behavior as the absolute values). As both oscillations are out of phase, they cancel out the global OH*-emission oscillations, which consequently do not exhibit a dominant peak in the OH* spectrum plotted in Fig. 14. Thus, at this frequency, the flame has a damping effect on the global OH* emissions. The phase averaging is also performed at the first harmonic of the forcing frequency (i.e., 240 Hz). The flame evolution shown in Fig. 17 depicts a similar pattern as the structure described previously, with the difference being that the spatial wavelength is approximately three times smaller.

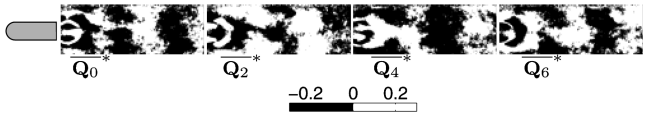

Fig. 17 Phase averaging of the raw snapshots at the first harmonic of the forcing frequency (i.e., 240 Hz).

2. *Improvement of Structure Visualization by Phase Averaging of Proper Orthogonal Decomposition Reconstructed Snapshots*

For comparison, POD analysis is performed on the same data set. The six dominant resulting modes are shown in Fig. 18. The shape of the first two modes is very similar to the shape of the phase-averaged images of Fig. 16. The same is true when modes 5 and 6 are compared, which show similar short wavelength structures as the phase-averaged images at 240 Hz. Modes 3 and 4 correspond to the frequency peak around 57 Hz. Because of the peak shape, these spatial modes remain very noisy and do not show a clear pattern, except a visible symmetry relative to the plane $y/h = 0$.

The eigenvalues of the unforced and forced cases, presented in Fig. 19, show a distinct difference between the two cases. The eigenvalues of the unforced case (·) are more homogeneously distributed, the maximum value remaining below 5% of the contribution to the OH* emission, and at least 52 modes are needed to reconstruct 50% of the original information. The forced case (×) shows two dominant modes that can, together, reconstruct more than 20% of the OH* emission. In all, only 22 modes are required to reconstruct 50% of the original information. As a result, their mode

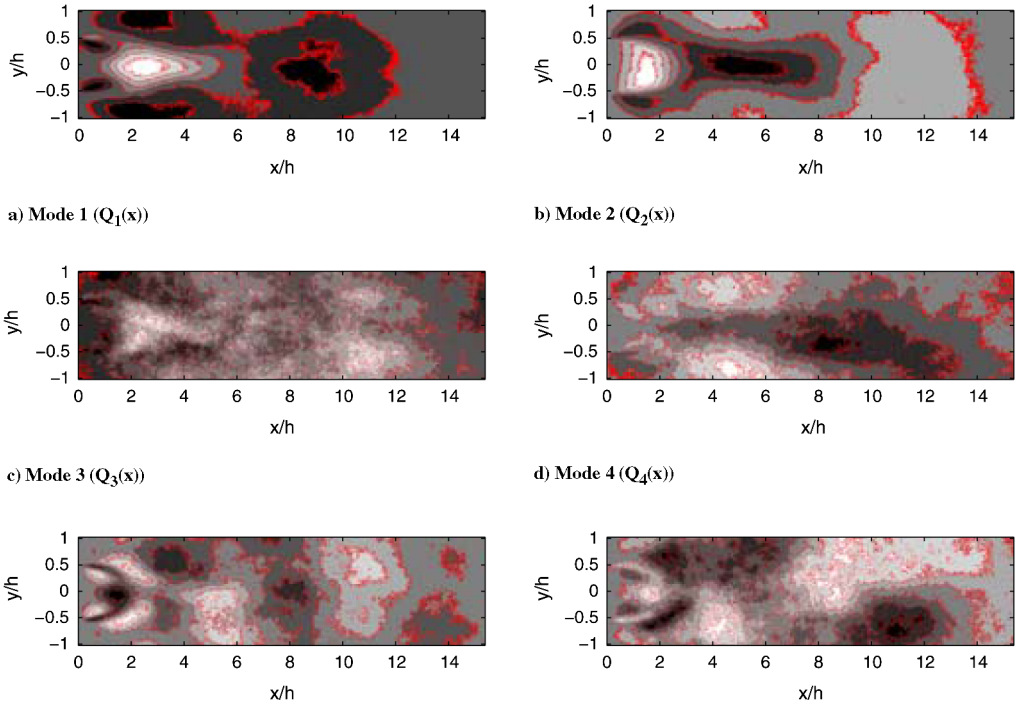

Fig. 18 POD modes of the flow forced at 120 Hz (see power spectrum density in Fig. 14).

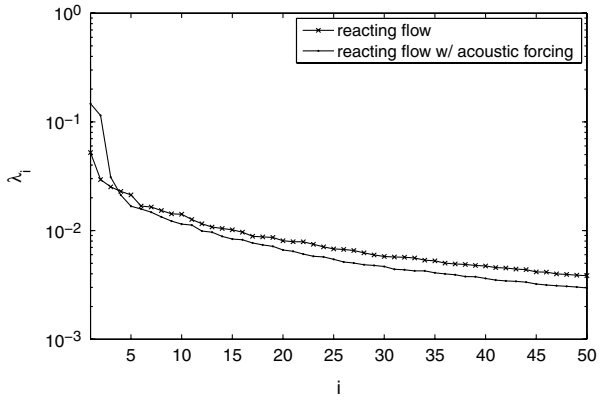

Fig. 19 Eigenvalues of the POD analysis for the natural and forced cases (120 Hz).

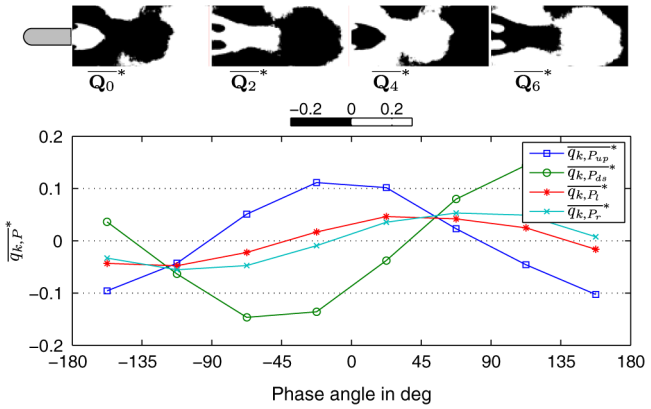

Fig. 20 Phase reconstruction of the POD-filtered snapshots using the first two modes. Forcing at 120 Hz.

shapes are better resolved, as shown in Fig. 18, and a low-dimensional reconstruction is expected to give a better visualization of the flame dynamics. This is in accordance with the reconstruction resulting from the first two POD modes depicted in Fig. 20. When compared with the reconstruction performed with the raw snapshots, the structure shapes remain identical, with a smoother profile for the flame reconstructed after POD filtering. The advantage of the POD filter becomes obvious when looking at the reconstruction at 240 Hz (Fig. 21). The spatial modes 3 to 20 are used to reconstruct the snapshots, as the first two modes corresponded to the forcing frequency. There, the flow structures are much clearer than in the case for the direct phase-averaging procedure (see Fig. 17).

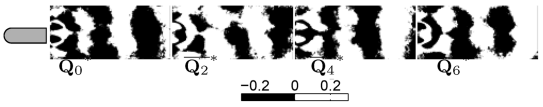

Fig. 21 Phase reconstruction of the POD-filtered snapshots using the modes 3 to 20 at the frequency of 240 Hz. Forcing at 120 Hz.

V. Coherent Structures in a Swirl Burner

The same methods as used previously are applied to the complex flame of the swirl-stabilized burner. The influence of the camera viewing angle is studied in Sec. V.A. The different combustor modes are then reconstructed (Sec. V.B). Finally, the influence of acoustic forcing on the helical mode is investigated (Sec. V.C).

A. Impact of a Nonrotational Symmetric Flame Shape on the Image Recording

Because the flame is not axisymmetric, the shape recorded by the camera strongly depends on the viewing angle θ between the camera and the burner inlet slots plane. Two positions of the camera relative to the burner are investigated ($\theta = \theta_1 = \frac{\pi}{2}$ or $\theta = \theta_2 = 0$). The resonance tube of the combustion chamber is removed to ensure a stable combustion. Except the change in the viewing angle, all other parameters are kept constant between the two tests.

The mean OH* emission for the two angles, θ_1 and θ_2, presented in Fig. 22, show how strongly the recorded flame shape changes with the viewing angle. These differences lead to strong deviations when phase averaging of the snapshots is performed, as shown in Figs. 23 and 24. For the operating conditions and the acoustic boundary conditions considered, a single dominant peak at 170 Hz is observed in the pressure and OH* spectra. Phase averaging is therefore performed at this frequency. The pictures of Fig. 23, as well as the integrated intensities on the left side $\overline{q_{k,\mathcal{P}_l}}^*$ and on the right side $\overline{q_{k,\mathcal{P}_r}}^*$, reveal an oscillating motion of the heat release between the y^- and the y^+ sides, characterized by a 180° phase shift between both sides. This indicates a rotating motion around the flow axis that is characteristic of helical structures. On the contrary, the pictures in Fig. 24 appear to be much more noisy, and the intensities $\overline{q_{k,\mathcal{P}_l}}^*$ and $\overline{q_{k,\mathcal{P}_r}}^*$ do not clearly show a 180° phase shift between the left and the right planes.

To see whether more information can be extracted from the noisy data of the second viewing angle, POD filtering is applied. For comparison, the eigenvalues of the 20 first modes for both viewing angles are presented in Fig. 25. The snapshot complexity is visible in the relative energy contained in those 20 modes: 52% for viewing angle θ_2 and 60% for viewing angle θ_1. For both cases, more than 250 modes are needed to resolve more than 90% of the total energy. The first two modes of the viewing angle θ_1 comprise 10% more energy than the first two modes of θ_2. This may explain why the phase averaging of the single snapshot is smoother for the viewing angle θ_1. Nevertheless, the snapshot reconstruction with the first two POD modes for θ_2, shown in Fig. 26, reveals a smoothened helical structure. The filtered intensities of $\overline{q_{k,\mathcal{P}_l}}^*$ and $\overline{q_{k,\mathcal{P}_r}}^*$ also display an

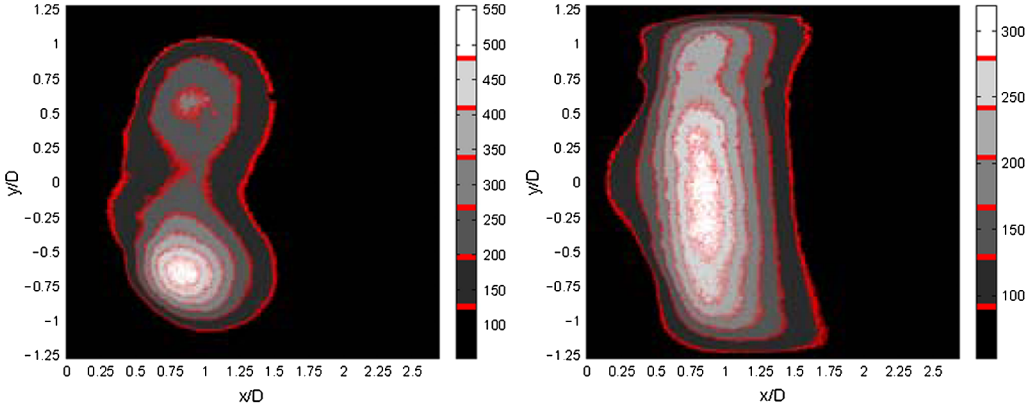

Fig. 22 Mean OH* chemiluminescence of natural flame for two viewing angles: $\theta_1 = \frac{\pi}{2}$ (left) and $\theta_2 = 0$ (right).

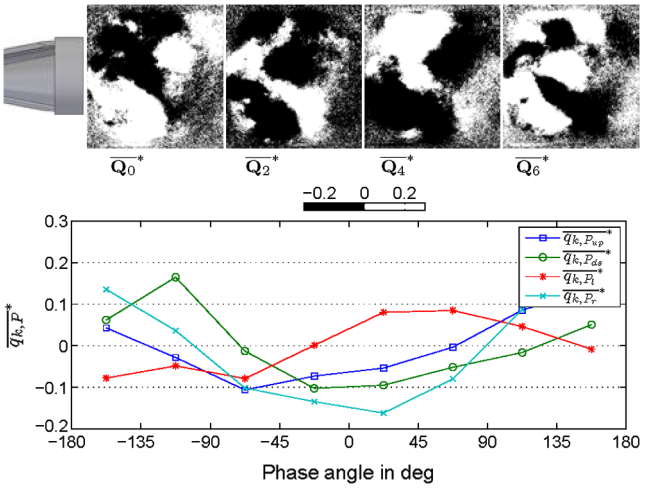

Fig. 23 Phase reconstruction of the flame, $\theta_1 = \pi/2$, natural flow.

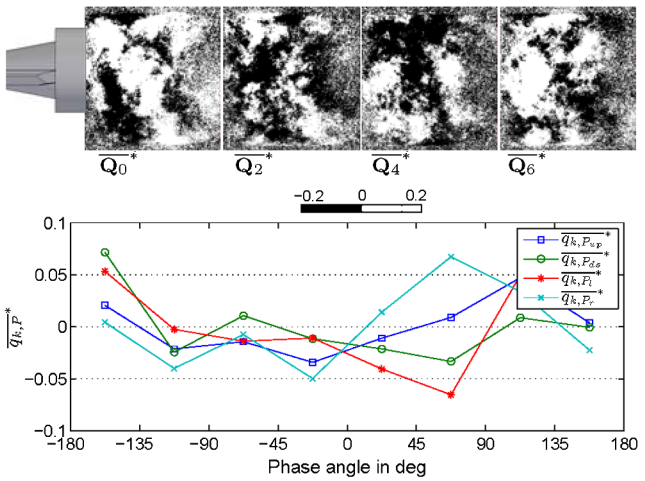

Fig. 24 Phase reconstruction of the flame, $\theta_2 = 0$, natural flow.

oscillation out of phase. Hence, even if the raw snapshot phase averaging does not lead to satisfying results, the snapshots reconstructed with POD and phase averaging allows the extraction of the dominant natural flow structure.

To further illustrate the POD filtering, four raw snapshots are compared with their corresponding filtered counterparts (projection

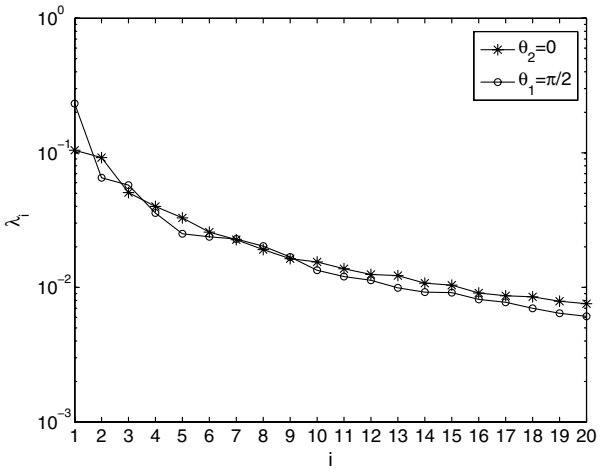

Fig. 25 Eigenvalues of chemiluminescence snapshots for $\theta = \theta_1$ and $\theta = \theta_2$. The first two modes of the angle of view θ_1 resolve 29.7% of the total energy, while the first two modes of the angle of view θ_2 resolve only 19.7% of the total energy.

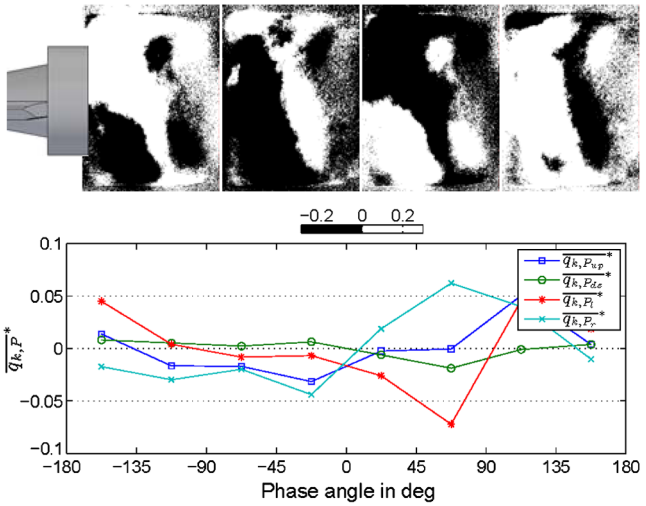

Fig. 26 Phase reconstruction of the flame, $\theta = \theta_2$, with the first two modes of the POD analysis.

onto the first two dominant modes) in Fig. 27. Even if the instantaneous camera pictures are noisy, they obviously present similar patterns as the filtered ones.

B. Modes of the Flame in the Combustor

The phase-averaging method of the raw snapshots is applied to visualize the different mode shapes in the combustor corresponding to the power spectrum shown in Fig. 6. For these operating conditions, the flow is forced with the loudspeaker at 150 Hz, which causes the distinct peak in the power spectrum. The two other modes are natural modes of the combustor, the first peak around 75 Hz corresponding to an acoustic quarter wave mode, the third being the typical flow instability mode of the burner, already visualized in Figs. 23 and 24.

For these investigations, the viewing angle of the camera is set to $\theta = \pi/4$, and 280 snapshots for each measurement are recorded. This number was chosen as a compromise between the measurement time at each operating point and the quality of the phase-averaged measurements. Since the phase averaging of the raw snapshots exhibited a fair quality, no POD filtering was applied. Figures 28–30 show the phase-averaged pictures resulting from the same data set of 280 pictures. Their analysis extracts the impact of the modes on the flame shape in the combustor. Figure 28 shows that the whole flame is oscillating in phase over one cycle of the frequency of 75 Hz, which corresponds to a standing wave (i.e., the spatial pressure field in the combustor is oscillating in phase). There is no region of the flame that adds heat fluctuations out of phase. Hence, if pressure oscillations in the combustor are in phase with the heat release, a strong thermo-acoustic instability can occur. To stabilize the latter, either the phase between heat release and pressure oscillations has to be adjusted, or the amplitude of pressure oscillations has to be dampened (for example, by decreasing the magnitude of the reflection coefficient at the combustor outlet).

The forced oscillation mode at 150 Hz in Fig. 29 reveals a traveling wave through the flame, similar to the traveling wave of the bluff-body flame. A stronger OH* emission originates in the center, just downstream of the burner for $\bar{\mathbf{Q}}_4^*$, and propagates downstream as well as to the left and right of the picture ($\bar{\mathbf{Q}}_0^*$). A phase shift of around 180° between $\overline{q_{k,\mathcal{P}_{up}}}^*$ and $\overline{q_{k,\mathcal{P}_{ds}}}^*$ is also present. The analysis of the phase-averaged snapshots at a frequency of 170 Hz reveals the helical structure of the flame, as observed in the previous section.

The presented postprocessing method thus allows the visualization and reconstruction of the different combustor modes with only one set of snapshots and an appropriate phase-sorting algorithm. The analysis of the results reveal different mode shapes across the flame and give a better insight into the physical mechanisms of combustion instabilities.

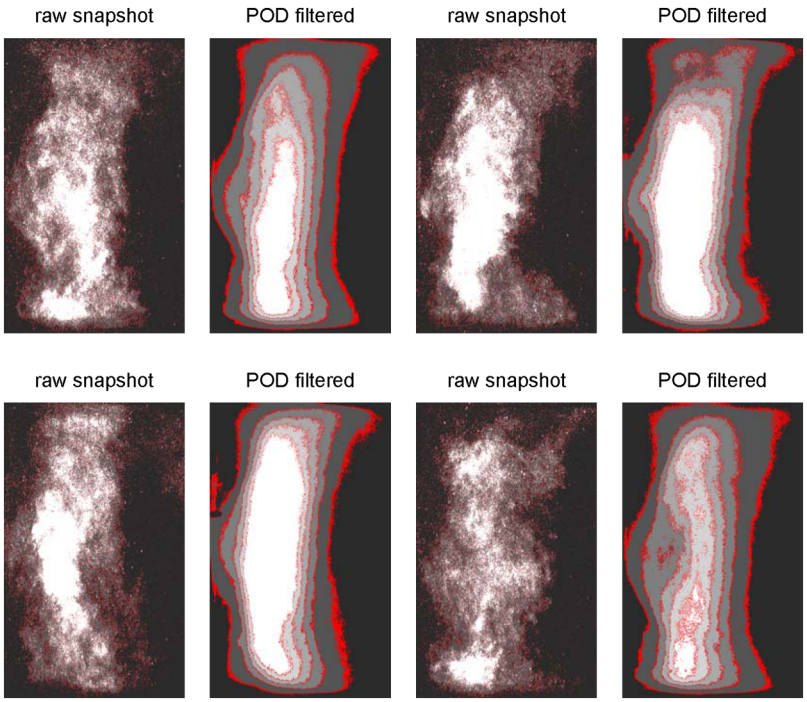

Fig. 27 Comparison of the raw OH* snapshots with the corresponding POD filtered snapshots for the viewing angle $\theta = \theta_2$.

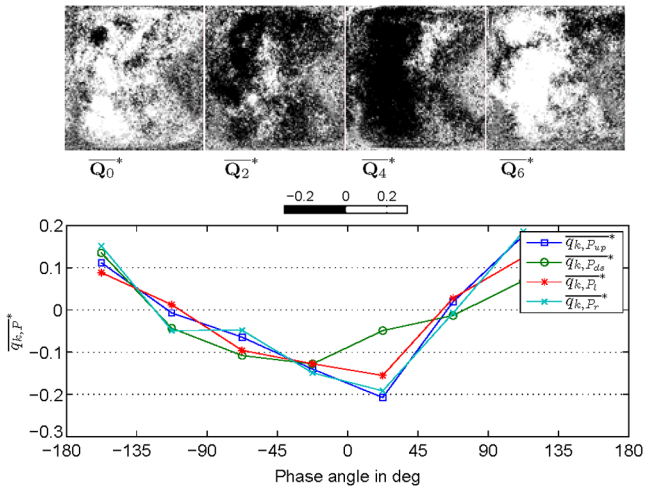

Fig. 28 Phase reconstruction at 75 Hz, axisymmetric structure.

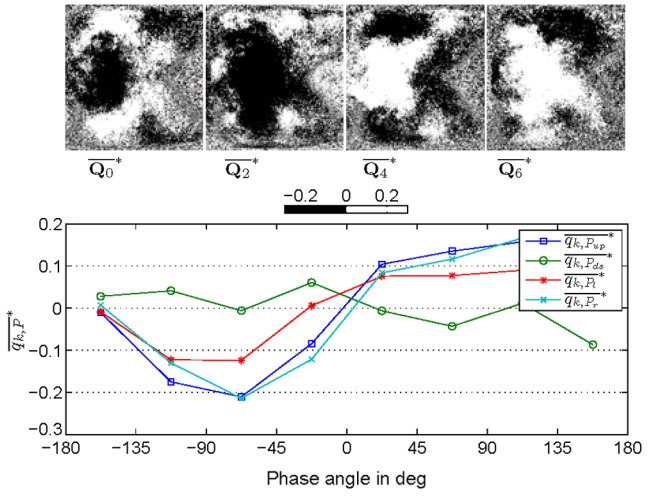

Fig. 29 Phase reconstruction at 150 Hz, axisymmetric structure.

C. Effect of Acoustic Forcing on the Helical Structure

To investigate the effect of acoustic forcing on the natural helical flow structure, the system was excited with the upstream loudspeaker. The left column of Fig. 31 shows the influence of loudspeaker excitation on the coherence between the two photomultiplier signals. The forcing frequency was adjusted to 170 Hz, corresponding to the observed natural frequency of the helical flow instability. The excitation amplitude u_{exc} is increased from top (0 V) to bottom (0.7 V). The coherence C_{xy} of two signals, x and y, is defined as

$$C_{xy} = \frac{|P_{xy}|^2}{P_{xx}P_{yy}} \tag{9}$$

where P_{xy} denotes the cross-power spectral density of x and y, and P_{xx} and P_{yy} are the power spectral densities of the autocorrelations of x and y, respectively. The coherence, therefore, can take values ranging from zero to one: one representing the case of completely correlated signals. The higher the coherence, the more the two signals are related to each other.

As in the previous section, the two characteristic frequency ranges of the governing modes (around 70 and 170 Hz) can be observed.

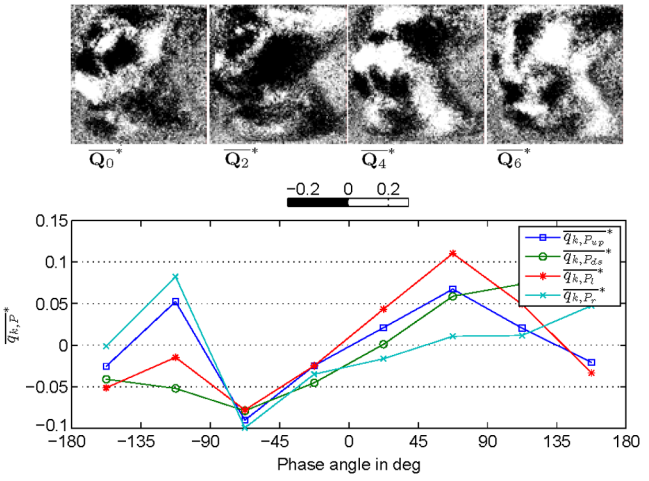

Fig. 30 Phase reconstruction at 170 Hz, helical structure.

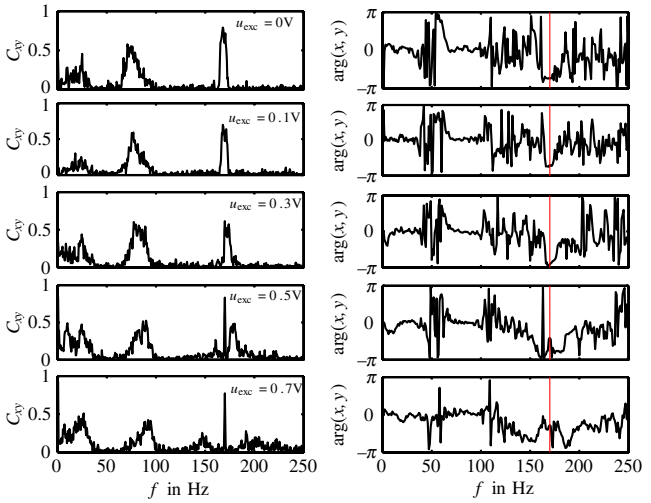

Fig. 31 Coherence (left) and phase difference in rad (right) between photomultiplier signals *x* and *y*. The excitation amplitude of the loudspeaker is continuously increased from top to bottom. Acoustic forcing at 170 Hz.

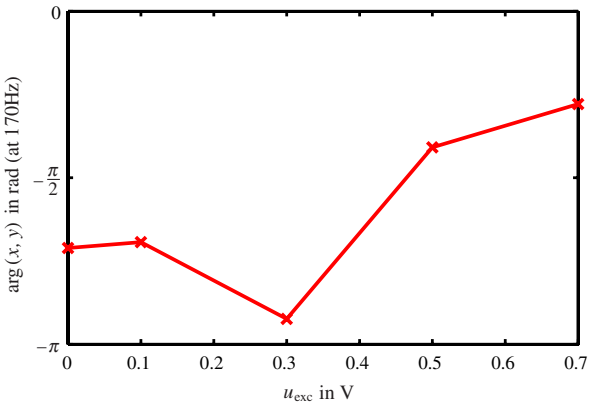

Fig. 32 Phase difference between photomultiplier signals *x* and *y* over excitation amplitude at forcing frequency 170 Hz.

At these frequencies, the photomultiplier signals show the highest coherence. We will now concentrate on the frequency of the helical flow instability at 170 Hz. Up to an excitation amplitude of 0.3 V, no significant influence is seen. The forcing amplitude seems to be too small to have an effect on the flow structure when compared with the uncontrolled case. Further increasing of the excitation amplitude, however, results in a change of the coherence signal. At 0.5 and 0.7 V, the shape of C_{xy} changes, and at 0.7 V, only a sharp peak at the forcing frequency is observed. In the same time, two much weaker peaks appear on both sides of the 170 Hz peak. Their distance to the stronger one increases with increasing forcing amplitude, while their amplitudes decrease. To understand the underlying physical mechanisms, consider the phase of C_{xy}, shown on the right column of

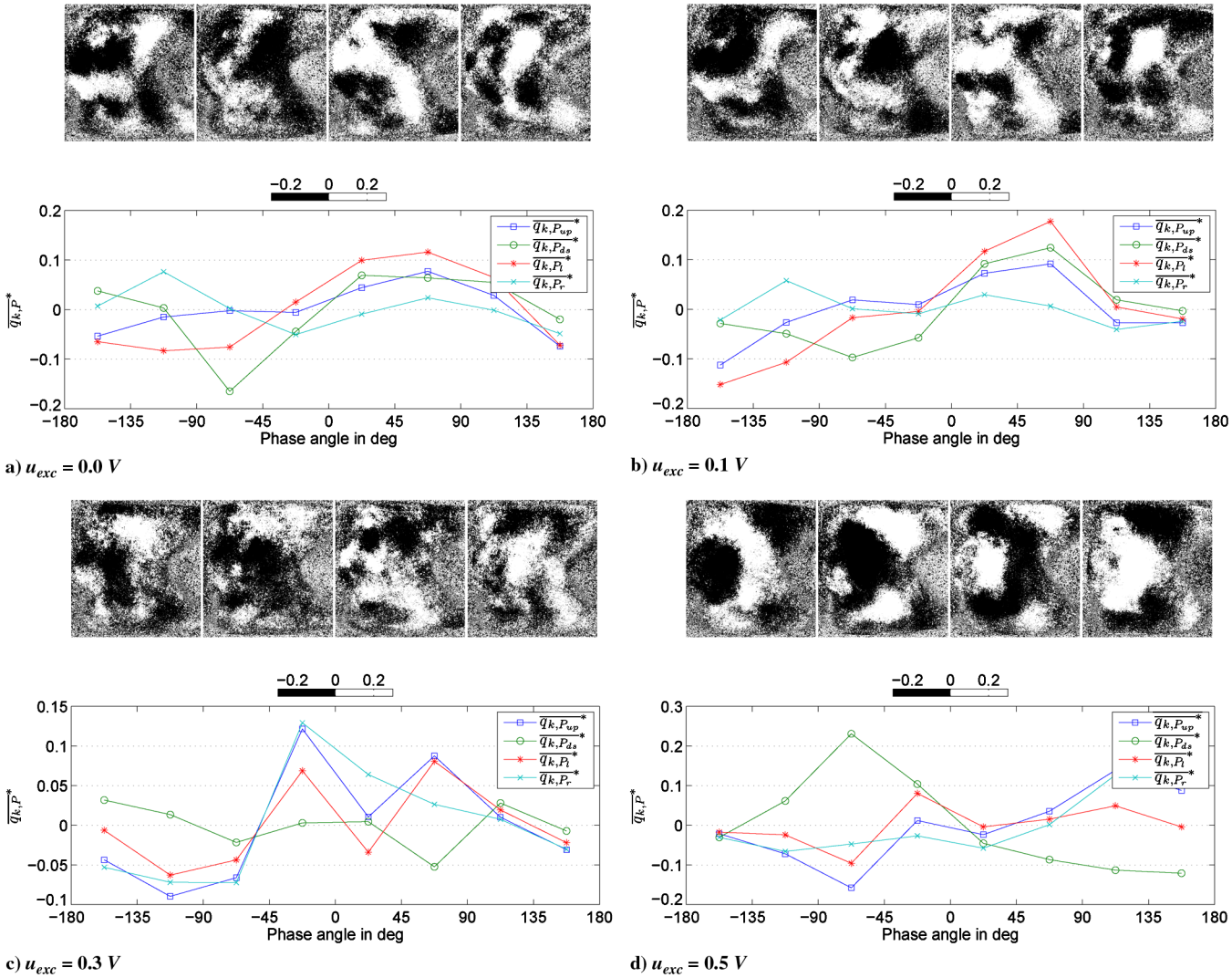

a) u_{exc} **= 0.0 *V***

b) u_{exc} **= 0.1 *V***

c) u_{exc} **= 0.3 *V***

d) u_{exc} **= 0.5 *V***

Fig. 33 Phase-averaged snapshots of the relative heat release when axial forcing is applied at 170 Hz at four amplitudes (also shown in Fig. 31).

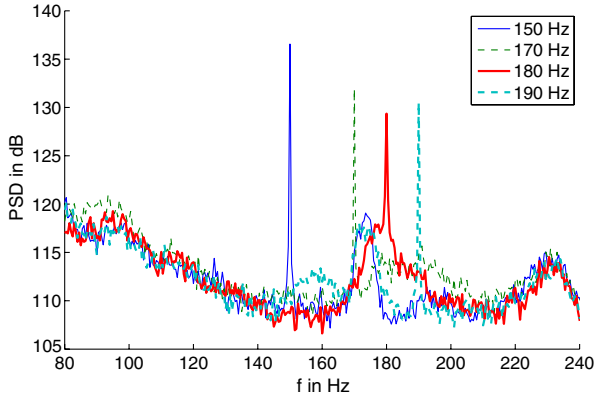

Fig. 34 Power spectrum density (PSD) of the OH* integral signal, showing the impact of different forcing frequencies on the peak of the helical structure. A weak lock-in phenomenon is observed.

Fig. 31. For the cases of small excitation amplitudes, a phase of approximately −2.5 rad is observed around 170 Hz. This value is close to the phase difference of $\pm\pi$, which is expected for a helical structure. The deviation of the observed phase difference to $-\pi$ can be attributed to the fact that the photomultipliers are not focused to only one point and that the flow structure is highly unsteady. Increasing the forcing amplitude to 0.7 V results in a decrease of the phase difference to approximately −0.8 rad (i.e., a phase difference of a quasi-axial flow separation). In Fig. 32, the trend of the phase difference with the forcing amplitude at 170 Hz is shown (analogous to the vertical lines in Fig. 31). The natural helical flow structure is replaced at high-forcing amplitudes at this frequency by an axial structure. This does not mean that the helical structure is completely destroyed. The peaks situated on both sides of the 170 Hz peak in Fig. 31 indeed show a phase very close to the initial phase when no or low forcing is applied. As the dominant POD modes of the snapshots also showed antisymmetric shapes, this suggests that the axial forcing at 170 Hz shifts helical modes to higher or lower frequencies.

It was not clear whether the outlier at 0.3 V has to be attributed to measurement uncertainties or to the fact that the helical structure is enhanced when compared with the case without control. Phase averaging of the raw snapshots was performed, and results are presented in Fig. 33. The pictures clearly confirm that the coherent structure changes from a helical shape at a low-forcing amplitude to an axisymmetric above 0.5 V. The 0.3 V forcing case does not show clear structure patterns when looking at the pictures or at the curve of $\overline{q_{k,\mathcal{P}}}^*$. The transition from the low-forcing amplitude structures to the high-forcing amplitude structures can thus be seen as the coexistence of axial, as well as helical, structures at 170 Hz. This fact could explain the occurrence of the outlier at 0.3 V.

Tests were also conducted to investigate an eventual lock-in phenomenon of the helical structure on the forcing frequency. The flame was forced with a loudspeaker voltage of 0.5 V at four frequencies (150, 170, 180, and 190 Hz) surrounding the frequency of the helical mode. As shown in Fig. 34, the peak of the helical structure remains almost unchanged for the 150 and 190 Hz cases, while it completely disappears for a forcing at 170 Hz. Only for a forcing at 180 Hz did the helical structure peak move slightly to higher frequencies. Thus, except for forcing frequencies close to the natural frequency of the helical structure, it is only marginally affected by harmonic forcing of high amplitude.

VI. Conclusions

The postprocessing techniques presented in this paper successfully combine phase reconstruction and phase averaging of OH*-chemiluminescence snapshots with POD to enhance the visualization of coherent flame structures in premixed flames. With a relatively small number N of snapshots ($N < 300$ for some cases), the evolution of the dominant modes can be well reconstructed by phase averaging either of the raw snapshots or the POD-filtered snapshots. This allows the reduction of the measurement time, as well as the amount of data. At the same time, more dynamic information is available when compared with standard onsite phase-locked measurements.

The method was applied to two different premixed flames: a bluff-body stabilized flame and a swirl-stabilized flame of an industrial burner. For the first case, the phase-reconstructed snapshots show an axisymmetric structure, shedding from the trailing edge of the bluff body. This structure suppresses the asymmetrical von Kármán vortex street of the nonreacting case, confirming previous numerical investigations made on a similar configuration. The data recorded on the swirl-stabilized flame capture the typical helical structure very well and shows how acoustic forcing at different frequencies and amplitudes influences its evolution. In particular, when forcing is applied at the frequency of the helical structure, a transition from a helical mode to an axisymmetric one occurs, depending on the amplitude of forcing.

Acknowledgment

The authors thank the German Science Foundation (DFG) for the financial support of this work within the collaborative research center 557 titled, “Control of complex turbulent shear flows.”

References

[1] Crocco, L., and Cheng, S., “Theory of Combustion Instability in Liquid Propellant Rocket Motors,” AGARDograph 8, Butterworths, London, 1956.

[2] Keller, J. J., “Thermoacoustic Oscillations in Combustion Chambers of Gas Turbines,” *AIAA Journal*, Vol. 33, No. 12, 1995, pp. 2280–2287. doi:10.2514/3.12980

[3] Lieuwen, T., and Yang, V., *Combustion Instabilities in Gas Turbine Engines*, Vol. 210, Progress in Astronautics and Aeronautics, AIAA, Reston, VA, 2006.

[4] Poinsot, T., Veyante, A. T. D., Candel, S., and Esposito, E., “Vortex Driven Acoustically Coupled Combustion Instabilities,” *Journal of Fluid Mechanics*, Vol. 177, 1987, pp. 265–292. doi:10.1017/S0022112087000958

[5] Paschereit, C. O., Gutmark, E. J., and Weisenstein, W., “Coherent Structures in Swirling Flows and Their Role in Acoustic Combustion Control,” *Physics of Fluids*, Vol. 11, No. 9, 1999, pp. 2667–2678. doi:10.1063/1.870128

[6] Schadow, K. C., and Gutmark, E. J., “Combustion Instability Related to Vortex Shedding in Dump Combustors and Their Passive Control,” *Progress in Energy and Combustion Science*, Vol. 18, No. 2, 1992, pp. 117–132. doi:10.1016/0360-1285(92)90020-2

[7] Lacarelle, A., Faustmann, T., Greenblatt, D., Paschereit, C. O., Lehmann, O., Luchtenburg, D. M., and Noack, B. R., “Spatiotemporal Characterization of a Conical Swirler Flow Field Under Strong Forcing,” *Journal of Engineering for Gas Turbines and Power*, Vol. 131, No. 3, 2009, p. 031504. doi:10.1115/1.2982139

[8] Paschereit, C. O., Gutmark, E. J., and Weisenstein, W., “Excitation of Thermoacoustic Instabilities by Interaction of Acoustics and Unstable Swirling Flow,” *AIAA Journal*, Vol. 38, No. 6, 2000, pp. 1025–1034. doi:10.2514/2.1063

[9] Paschereit, C. O., and Gutmark, E., “Control of High Frequency Thermoacoustic Pulsations by Distributed Vortex Generators,” *AIAA Journal*, Vol. 44, No. 3, 2006, pp. 550–557. doi:10.2514/1.21192

[10] Paschereit, C. O., and Gutmark, E. J., “Proportional Control of Combustion Instabilities in a Simulated Gas-Turbine Combustor,” *Journal of Propulsion and Power*, Vol. 18, No. 6, 2002, pp. 1298–1304. doi:10.2514/2.6067

[11] Li, F., Tadmor, G., Noack, B. R., Banaszuk, A., and Mehta, P. G., “A Reduced Order Galerkin Model for the Reacting Flameholder,” 3rd AIAA Flow Control Conference, AIAA Paper 2006-3487, June 2006, 2006.

[12] Ihrke, I., and Magnor, M., “Image-Based Tomographic Reconstruction of Flames,” *Proceedings of the 2004 ACM SIGGRAPH/Eurographics Symposium on Computer Animation*, edited by, D. K. Pai and R. Boulic, Eurographics Assoc., Aire-la-Ville, Switzerland, 2004, pp. 365–373. doi:10.1145/1028523.1028572

[13] Berkooz, G., Holmes, P., and Lumley, J., “The Proper Orthogonal Decomposition in the Analysis of Turbulent Flows,” *Annual Review of*

Fluid Mechanics, Vol. 25, No. 1, 1993, pp. 539–575.
doi:10.1146/annurev.fl.25.010193.002543

[14] Bonnet, J., Cole, D., Delville, J., Glauser, M., and Ukeiley, L., "Stochastic Estimation and Proper Orthogonal Decomposition: Complementary Techniques for Identifying Structure," *Experiments in Fluids*, Vol. 17, No. 5, 1994, pp. 307–314.
doi:10.1007/BF01874409

[15] Edwards, J. L., Gouldin, F. C., Grinstein, F. F., and Kailasanath, K., "Reduced-Order Structure of Reacting Rectangular Jets," *AIAA Journal*, Vol. 43, No. 5, 2005, pp. 1075–1087.
doi:10.2514/1.6426

[16] Gabor, D., "The Theory of Communication," *Journal of the Institution of Electrical Engineers, Part 3: Radio and Communication Engineering*, Vol. 93, No. 26, 1946, pp. 429–457.

[17] Güthe, F., and Schuermans, B., "Phase-Locking in Post-Processing for Pulsating Flames," *Measurement Science and Technology*, Vol. 18, No. 9, 2007, pp. 3036–3042.
doi:10.1088/0957-0233/18/9/039

[18] Oudheusden, B., Scarano, F., Hinsberg, N., and Watt, D., "Phase-Resolved Characterization of Vortex Shedding in the Near Wake of a Square-Section Cylinder at Incidence," *Experiments in Fluids*, Vol. 39, No. 1, 2005, pp. 86–98.
doi:10.1007/s00348-005-0985-5

[19] Perrin, R., Braza, M., Cid, E., Cazin, S., Barthet, A., Sevrain, A., Mockett, C., and Thiele, F., "Obtaining Phase Averaged Turbulence Properties in the Near Wake of a Circular Cylinder at High Reynolds Number Using POD," *Experiments in Fluids*, Vol. 43, No. 2, 2007, pp. 341–355.
doi:10.1007/s00348-007-0347-6

[20] Shannon, D., and Morris, S., "Experimental Investigation of a Blunt Trailing Edge Flow Field with Application to Sound Generation," *Experiments in Fluids*, Vol. 41, No. 5, 2006, pp. 777–788.
doi:10.1007/s00348-006-0200-3

[21] Sattelmayer, T., Felchlin, M. P., Haumann, J., Hellat, J., and Styner, D., "Second-Generation Low-Emission Combustors for ABB Gas Turbines: Burner Development and Tests at Atmospheric Pressure," *Transactions of the American Society of Mechanical Engineers*, Vol. 114, No. 1, 1992, pp. 118–124.
doi:10.1115/1.2906293

[22] Doebbeling, K., Knoepfel, H. P., Polifke, W., Winkler, D., Steinbach, C., and Sattelmayer, T., "Low NO_x Combustion of MBTU Fuels Using the ABB Double Cone Burner (EV Burner)," Proceedings of the International Gas Turbine and Aeroengine Congress and Exposition, American Society of Mechanical Engineers Paper 94-GT-394, Fairfield, NJ, 1994.

[23] Bothien, M. R., Moeck, J. P., and Paschereit, C. O., "Active Control of the Acoustic Boundary Conditions of Combustion Test Rigs," *Journal of Sound and Vibration*, Vol. 318, Nos. 4–5, 2008, pp. 678–701.
doi:10.1016/j.jsv.2008.04.046

[24] Dussault, D., and Hoess, P., "Noise Performance Comparison of ICCD with CCD and EMCCD Cameras," *Proceedings of SPIE: The International Society for Optical Engineering*, Vol. 5563, 2004, pp. 195–204.

[25] Haber, L., "An Investigation into the Origin, Measurement and Application of Chemiluminescent Light Emissions from Premixed Flames," M.S. Thesis, Virginia Polytechnic Inst. and State Univ., Blacksburg, VA, 2000.

[26] Guethe, F., Lachner, R., Schuermans, B., Biagioli, F., Geng, W., Inauen, A., Schenker, S., Bombach, R., and Hubschmidt, W., "Flame Imaging on the ALSTOM EV-Burner: Thermo Acoustic Pulsations and CFD-Validation," 44th AIAA Aerospace Sciences Meeting and Exhibit, AIAA Paper 2006-437, Jan. 2006.

[27] Higgins, B., McQuay, M., Lacas, F., and Candel, S., "An Experimental Study on the Effect of Pressure and Strain Rate on CH Chemiluminescence of Premixed Fuel-Lean Methane/Air Flames," *Fuel*, Vol. 80, No. 11, 2001, pp. 1583–1591.
doi:10.1016/S0016-2361(01)00040-0

[28] Muruganandam, T. M., Kim, B., Olsen, R., Patel, M., Romig, B., and Seitzman, J. M., "Chemiluminescence Based Sensors for Turbine Engines," AIAA Paper 2003-4490, 2003.

[29] Schuermans, B., Guethe, F., and Mohr, W., "Optical Transfer Function Measurements for Technically Premixed Flames," American Society of Mechanical Engineers Paper GT2008-51500, 2008.

[30] Guyot, D., Moeck, J., Paschereit, C., and Schuermans, B., "Optical Transfer Function Measurement for a Premixed Swirl-Stabilized Flame at Atmospheric Conditions," AIAA Paper 2009-1236, 2009.

[31] Lacarelle, A., Matho, L., and Paschereit, C. O., "Sacalar Mixing Enhancement in a Swirl Stabilized Combustor Through Passive and Active Injection Control," AIAA Paper 2010-1332, 2010.

[32] Sirovich, L., "Turbulence and the Dynamics of Coherent Structures. Part 1: Coherent Structures," *Quarterly of Applied Mathematics*, Vol. 45, No. 3, 1987, pp. 561–571.

[33] Holmes, P., Lumley, J., and Berkooz, G., *Turbulence, Coherent Structures, Dynamical Systems and Symmetry*, Cambridge Univ. Press, Cambridge, England, U.K., 1998.

T. Jackson
Associate Editor